MEMS-enabled retrofitting of automobile wheel balancer for automatic unbalance detection

Gabriele Pozzato*, Silvia C. Strada*, Mara Tanelli*, Sergio M. Savaresi*, and Gerhard Dambach**

Abstract—The presence of asymmetries in the mass distribution of automobile tires causes anomalous forces and torques, which lead to vibrations and to ride disturbances. For this reason, detection of unbalanced masses is fundamental in order to perform a careful balancing, improving both safety and comfort. To this aim, traditional wheel balancers are passive devices that allow one to detect unbalances relying on force sensors. The major drawbacks of this technology are the high production costs and the loss of accuracy of the force sensors during the wheel balancer lifetime. In this work, a new sensors layout for the next generation of wheel balancers is proposed together with a structural modification of the machine that allows us to magnify the information provided by the sensors. Notably, these modifications are quite practical, and allows retrofitting traditional machines. The goal is to prove the effectiveness of accelerometers and gyroscopes, which are low-cost devices requiring minimum calibration effort, for unbalance detection purposes. To this aim, an unbalance detection algorithm is developed. Starting from the amplitudes and phases of the signals acquired by the sensors, the severity and the angular position of the unbalance is determined relying on a regression model. Then, the proposed detection strategy is experimentally tested in different unbalance conditions.

Index Terms—Wheel balancer, unbalance detection, balancing, MEMS, Industry 4.0

I. INTRODUCTION

Everyday vehicles are characterized by a considerable number of rotating parts, for which smooth running is essential. Components, such as crankshafts and turbines, need to be optimally balanced in order to work without any flaw and nor to suffer from excessive wear and tear. As a matter of fact, each rigid body rotating about a fixed axis may show, due to the possible presence of asymmetries in its mass distribution, anomalous forces and torques which can lead to vibrations, noise, and increased wearing; this may even lead to destruction at high speeds [1]–[3]. To overcome this problem, a balancing of the rotating masses is of paramount importance. Considering *positive compensation*, balancing weights are applied directly to the rotor. Conversely, in *negative compensation* scenarios, some mass is removed by drilling or grinding [4].

Therefore, also the vehicle wheels must be balanced after a tire change or other maintainance operations. As a matter of fact, a proper wheel balance is fundamental to improve comfort, reduce vibrations, and prolong the tire lifetime. To this aim, wheels are mounted on a Wheel Balancer (WB). This machine, while making the wheel rotating, determines the mass, angle, and side of the rim to which balancing weights must be applied. The goal is to ensure the weight is evenly distributed throughout each of the wheels of the vehicle, so that they rotate smoothly. Indeed, espetially at high speeds, even a tiny imbalance can lead to large anomalous forces and torques, which can cause the wheel assembly to dangerously spin unevenly. Since the WB is generally operating at low speeds (below $5000\,\text{rpm}$), the rotor can be safely modeled as a rigid shaft which does not show any elastic deformation during operation [5]–[7]. Therefore, according to [8], any imbalance distribution can be balanced in two different planes. In this scenario, two principal types of unbalance may arise: *static* and *dynamic*. Static unbalance is defined as "the eccentricity of the center of gravity of a rotor, caused by a point mass at a certain radius from the centre of rotation", [9]. Thus, the presence of an unbalance in the rotating mass generates a harmonic force at the rotational speed ω, with the amplitude proportional to the unbalance severity and increasing with the square of the rotational speed [10]. In this scenario, the balancing is performed attaching compensatory weights to the rim, positioning them at $180\,\text{deg}$ and with identical radius. Figure 1 shows a generic static unbalance for a rotating body. On the other side, a pure couple unbalance arises when, according to [9], "two equal masses are placed symmetrically about the centre of gravity, but positioned at $180\,\text{deg}$ from each other". In this scenario, no eccentricity of the rotor center of gravity is shown but, when the rotor starts turning, a shift in the inertia axis is caused, leading to strong vibrations. An illustrative couple unbalance scenario is shown in the middle diagrams of Figure 1. If masses m_1 and m_2 are not equal, the
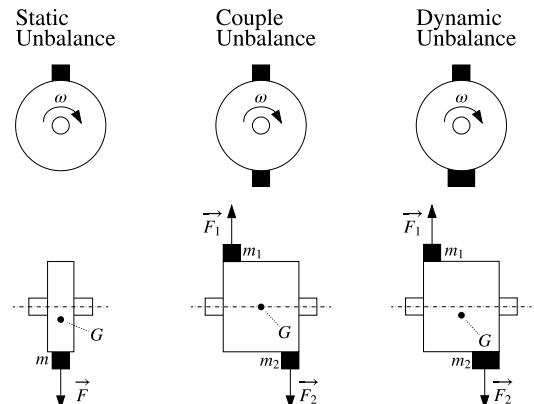
* G. Pozzato, S. C. Strada, M. Tanelli, and S. M. Savaresi are with the Dipartimento di Elettronica, Informazione e Bioingegneria, Politecnico di Milano, 20133 Milano, Italy. *e-mail: gabriele.pozzato@polimi.it*
** G. Dambach is with BSH Hausgeräte GmbH.

Fig. 1: Static, couple ($m_1 = m_2$), and dynamic ($m_1 \neq m_2$) unbalances.

(a) Static unbalance (outer plane)   (b) Static unbalance (inner plane)
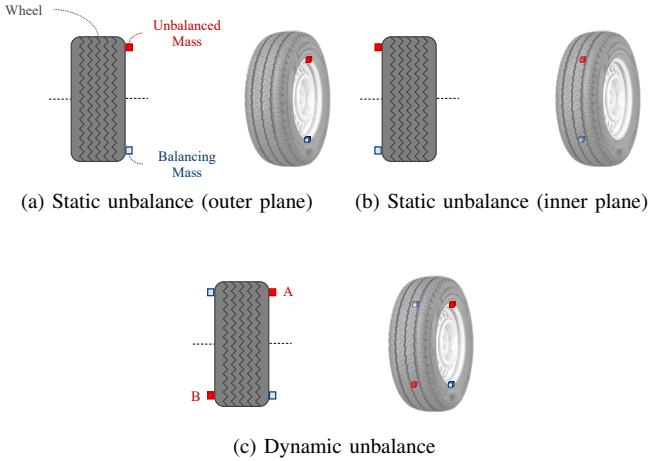
(c) Dynamic unbalance

Fig. 2: Static unbalance for the wheel outer (a) and inner (b) planes. The dynamic unbalance is shown in (c). If masses A and B are equivalent, a couple unbalance is obtained. Dark and pale colored masses highlight the unbalance and the balancing weights respectively.

rotor center of gravity shows eccentricity and the unbalance is called dynamic. Moreover, Figure 2 shows static and dynamic unbalances for a minivan wheel. In particular, dark and pale colored masses highlight the unbalance and the balancing weights respectively.

The WBs on the market rely on embedded electronics that evaluates the unbalance measuring the forces acting on the rotating shaft through piezoelectric devices. In [11], the authors present an experimental setup for vibrations measurement and imbalance fault detection in the context of a rotating machinery is presented using ceramic piezoelectric force sensors. The study in [12] proposes a method for wheel unbalance detection relying on a balancing machine capturing vibration signals through the charge outputs of two piezoelectric force sensors. Since car maintenance is becoming increasingly demanding, a remarkable drawback of piezoelectric force sensors is that they are prone to loose calibration and accuracy during the WB lifetime. Moreover, this technology is dated and force sensors are becoming much more expensive compared to today's standard Micro Electro-Mechanical Systems (MEMS) such as accelerometers and gyroscopes [13]. Therefore, the goal of this work is to develop an innovative wheel balancing solution, exploiting new, smart, and miniaturized sensors together with an *ad hoc* unbalance detection algorithm for the next generation of WBs. In practice, the detection of unbalanced masses is attained relying only on low-cost accelerometers and gyroscopes, easy to use sensing devices requiring a minimum calibration effort. To do this, a mechanical modification of the WB is proposed, which allows optimal exploitation of the sensors' capabilities. Further, an innovative unbalance detection algorithm is proposed and tested over different imbalance conditions, proving the effectiveness of MEMS technology. To the authors knowledge, this is the first time that gyroscopes are employed in this field. In conclusion, this is a successful example of engineering retrofit in Industry 4.0, for a machine designed in the 80s and updated introducing modern sensors'

Fig. 3: Bosch WBE 4430.

technology and a minimally-impacting mechanical redesign.

The remainder of the paper is organized as follows. Section II introduces and describes the experimental WB in its original, piezoelectric sensors based, configuration. Then, in Section III, the vibratory behavior of the in commerce WB is analyzed in time and frequency domains. In Section IV, some structural modifications of the machine are proposed in order to reduce its mechanical stiffness: this is necessary in order to enhance vibrations and make the detection of unbalances feasible from MEMS signals. Section V contains the core of the paper, in which a novel unbalance mass detection algorithm is described. Eventually, in Section VI the performances of the proposed algorithm are assessed by means of an extensive experimental campaign.

II. Measurement System Setup

The analysis in this work is based on a Bosch WBE 4430 (Figure 3). The machine is instrumented with two XDK programmable sensors[1], to assess the vibratory behavior of the structure by means of *3-dof* accelerometer and gyroscope measurements[2]. In a nutshell, the XDK platform is a wireless device which enables for rapid prototyping of sensor based products and applications for the Internet of Things (IoT). Therefore, accelerations and rotational speeds along $\{x, y, z\}$ (as defined by the fixed sensor reference frame of Figure 4) are acquired with a sampling frequency of $250\,\mathrm{Hz}$ (sampling time $T_s = 0.004\,\mathrm{s}$). Experimental tests are carried out considering a minivan wheel with a steel rim. The main characteristics of the WB, modeled as in Figure 4, and of the test wheel are summarized in Table I. In particular, the support is the mechanical component holding up the machine shaft. Therefore, the wheel is attached to the shaft, which rotates at the constant angular speed ω.

III. In Commerce WB Analysis

In order to assess the vibratory behavior of the WB currently in commerce, six different locations for the XDK sensor

---

[1]https://xdk.bosch-connectivity.com/

[2]The gyroscopes' sensitivity and range are $0.063\,(\deg/\mathrm{s})/\mathrm{LSB}$ (LSB indicates the Least Significant Bit) and $\pm 2000\,\deg/\mathrm{s}$. The accelerometers' sensitivity and range are $1.0 \times 10^{-3}\,\mathrm{G/LSB}$ and $\pm 16\,\mathrm{G}$.

Property	Value
Rim Diameter	$16''$ - 41 (cm)
Tire	215/64R16C
Shaft mass	11.0 (kg)
Wheel mass (tire+rim)	19.0 (kg)
Support mass	33.3 (kg)
Rotational speed (ω)	325 (rpm)

TABLE I: Wheel and WB properties.

SNR	
In commerce WB:	2.27 dB

Fig. 5: Spectral analysis of the x-axis acceleration measurements acquired by the fixed sensor **F**. A static unbalance of $100\,\mathrm{g}$ is considered. The presence of the unbalance is highlighted by the harmonic component at $5.4\,\mathrm{Hz}$ ($325\,\mathrm{rpm}$).

are tested. The idea is to determine which position shows the higher information content. Since the goal is to detect unbalances in the vehicle wheels, the information content is here measured as a signal energy difference between the unbalanced and balanced scenarios. In practice, Signal to Noise Ratio (SNR) [14] is computed

$$SNR = \frac{P_u}{P_b}, \qquad (1)$$

where P_u and P_b are the power of accelerations or angular velocities in the unbalanced and balanced scenario respectively. Therefore, the higher the SNR value, the higher the difference between balanced and unbalanced conditions, and the higher the chance to detect the unbalance. Using SNR as a cost function, two locations are selected:

- **F**: fixed position, *i.e.*, attached to the WB support;
- **R**: rotating position, *i.e.*, attached to the WB shaft and rotating with it at the rotational speed ω.
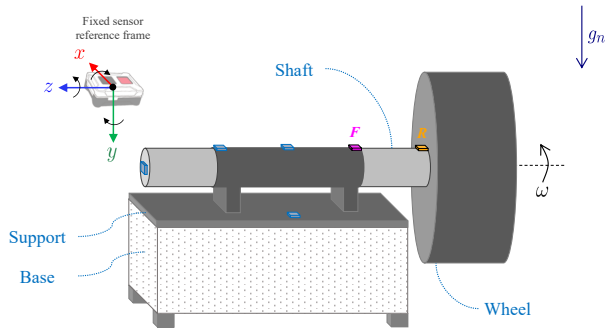

Fig. 4: Tested XDK sensor locations. **F** and **R** highlights the sensor positions with the higher information content. ω is the WB rotational speed and g_n is the gravitational acceleration. On the left, the fixed sensor reference frame is shown.

Figure 4 shows the tested locations together with the aforementioned most informative positions. The reference frame for the fixed XDK sensor is also shown. For the sake of completeness, the Power Spectral Density (PSD) [14] for the x-axis acceleration measurements, acquired by the fixed sensor, is shown in Figure 5. The presence of a static unbalance is highlighted by a harmonic component at the rotational speed of the WB (see also Appendix A), *i.e.*, at $325\,\mathrm{rpm}$ or $5.4\,\mathrm{Hz}$. It must be noticed that, in order to obtain the results of Figure 5, a static unbalanced mass of $100\,\mathrm{g}$ (far beyond a realistic wheel unbalance, usually around $35\,\mathrm{g}$) is introduced.

Thus, in order to enhance accelerations and angular velocities magnitudes for lower unbalance values, a reduction

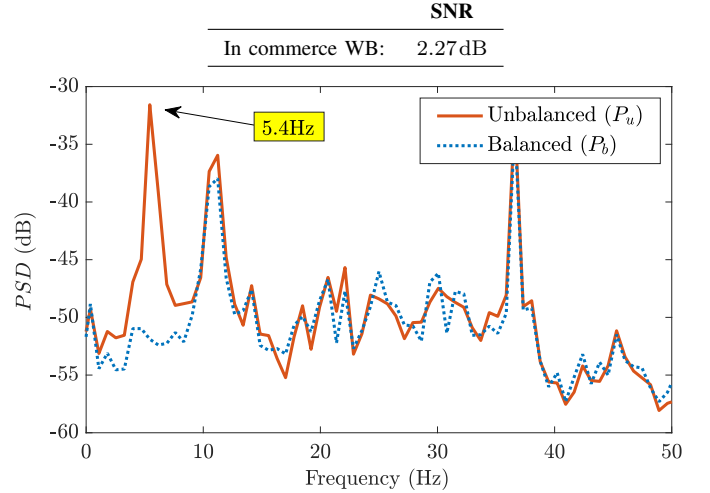of the machine structural stiffness is needed. Eventually, measurements acquired by the fixed (**F**) and the rotating (**R**) sensors are denoted respectively as

$$\{a_i^F(k), \omega_i^F(k)\}_{k=1,\ldots,N}$$
$$\{a_i^R(k), \omega_i^R(k)\}_{k=1,\ldots,N} \qquad (2)$$

with a_i and ω_i the accelerations and rotational speeds respectively, $i = \{x, y, z\}$ the sensor axes, and N the number of data points.

IV. Structural Stiffness Reduction

To reduce the mechanical stiffness of the WB, preliminary multi-body analysis (relying on MATLAB *Simscape Multibody™*) were performed in order to find configurations capable of enhancing vibrations with minimum changes of the in commerce WB structure. Specifically, flexibility is attained by means of $n_m = 4$ elastomer mounts placed in between the shaft support and the machine base (Figure 6). Thus, a careful sizing of these elastic elements is needed. Since the mounts are characterized by two different stiffness coefficients, depending whether the movement is along x (or, equivalently,
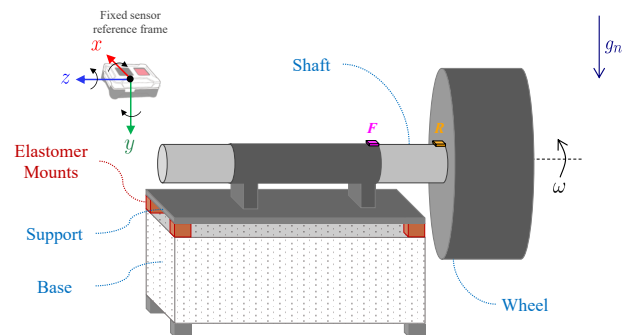

Fig. 6: Modified WB configuration. Four elastomer mounts are introduced between the shaft support and the machine base to reduce the structural stiffness.

Set	K_{wb}^x (kN/m)	K_{wb}^y (kN/m)
A	$n_m \times 66$	$n_m \times 600$
B	$n_m \times 54$	$n_m \times 400$
C	$n_m \times 28$	$n_m \times 173$

TABLE II: Stiffness coefficients along x (or z) and y for the sets of elastomer mounts A, B, and C. According to [15], the damping ratio ξ equals 10%. The $n_m = 4$ elastomer mounts are placed in the four corners of the shaft support.

z) or y (with respect to the fixed sensor reference frame), the analysis considers both the displacements. Three different sets of elastomer mounts, characterized by the properties highlighted in Table II, are tested. To assess the dynamic behavior of the WB, transfer functions between a force $F(t)$ and the displacements of the assembly support/shaft/wheel along x and y are computed. In practice, the idea is to approximate the WB of Figure 6 as a lumped sprung mass M_{wb} (given by the summation of shaft, wheel, and support masses), with lumped stiffness (K_{wb}^d), and damping (R_{wb}) coefficients. Therefore, the input/output relationship takes the following form

$$d(t) = G_d(s)F(t),$$
$$G_d(s) = \frac{\Omega_n^2}{s^2 + 2\xi\Omega_n s + \Omega_n^2},$$

where $\Omega_n = \sqrt{K_{wb}^d/M_{wb}}$ is the natural frequency, ξ the damping ratio, and $d = \{x, y\}$ the displacements.

The Bode diagrams for x and y displacements are depicted in Figure 7. Recalling that the rotation of the WB at $325\,\mathrm{rpm}$ generates a force at $5.4\,\mathrm{Hz}$ if a static unbalance is present, the elastomer mounts are selected in order to increase vibrations amplitudes while avoiding moving too close to the resonance peaks. As shown by Figure 7a, the force at $5.4\,\mathrm{Hz}$ is extremely close to the resonance peak of the Bode plot of configuration C, leading to potentially dangerous oscillations. Therefore, between set A and B, the stiffer one is chosen. This is a conservative solution to avoid high oscillations amplitude and potentially dangerous scenarios. In Figure 8, a_x^F measurements for the in commerce WB (stiff) and the reduced stiffness WB are compared. The SNR, with respect to the balanced scenario, is computed, showing an increased information content for the reduced stiffness WB acquisitions. Indeed, the introduction of elastomer mounts leads to a one order of magnitude increment for both accelerations and rotational speeds amplitudes, making the detection of unbalances feasible.

V. UNBALANCE DETECTION

In this section, an innovative algorithm for MEMS-based unbalance detection is proposed. First, the details of the testing procedure are presented, then, the detection algorithm is outlined.

A. Test description

Figure 9 depicts the modified WB with the $600\,\mathrm{kN/m}$ (stiffness along y) elastomer mounts (set A). The fixed and
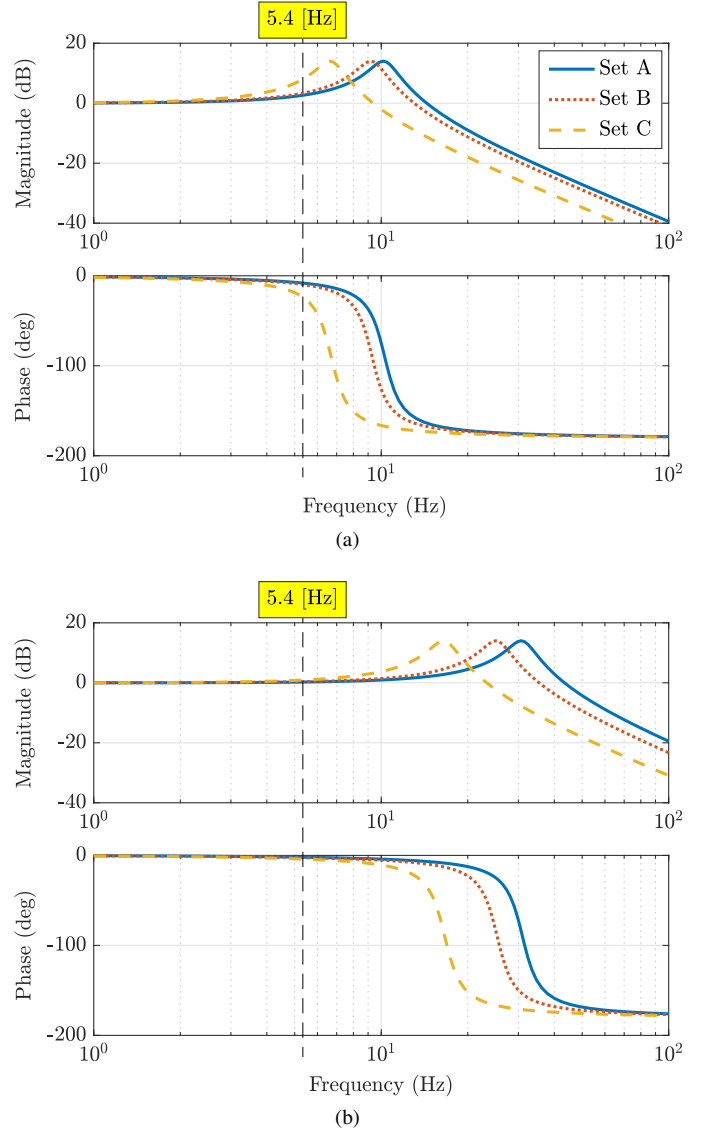

(a)

(b)

Fig. 7: Bode plots for (a) x and (b) y displacements. The external force is at $5.4\,\mathrm{Hz}$.

rotating XDK sensors are highlighted. The rotating XDK sensor is attached to the wheel at a distance of $10\,\mathrm{cm}$ from the axis of rotation, *i.e.*, the WB axle. Clearly, this introduces an unbalance which must be removed before the testing campaign. Thus, another XDK sensor, named *balancing*, is attached in opposite position, ensuring an almost perfect balancing. This sensor is not used to acquire data but is just needed for balancing purposes.

As mentioned in Section II, a *balanced* minivan wheel with a steel rim is used. Then, tests are performed introducing known unbalances by means of zinc tire weights ranging between 10 to $60\,\mathrm{g}$. Usually, unbalances higher than $60\,\mathrm{g}$ are caused, for instance, by rim deformations. In this scenario, the only options are substituting or repairing the rim (a balancing is not enough), which is out of the scope of this work. As a matter of fact, the main goal is to propose a procedure capable of detecting the severity and angular position of the unbalanced masses in order to perform a balancing. Thus, the algorithm
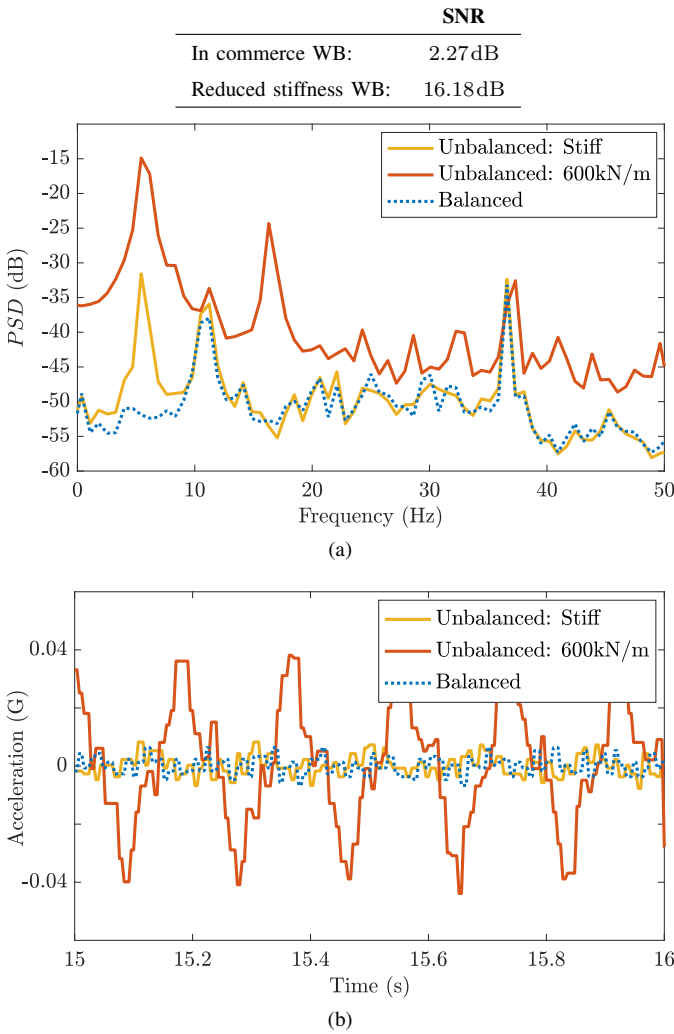
	SNR
In commerce WB:	$2.27\,\mathrm{dB}$
Reduced stiffness WB:	$16.18\,\mathrm{dB}$

(a)

(b)

Fig. 8: Comparison of PSD and time-domain a_x^F measurements for the in commerce WB and the reduced stiffness WB. A static unbalance of $100\,\mathrm{g}$ is considered. Acquired data are compared to the balanced baseline, showing the higher information content of accelerations acquired in the reduced stiffness scenario.

is developed considering two principal scenarios: a pure static unbalance and a pure couple unbalance (see again Figure 2). The study is focused on static and couple unbalances because the objective is to show whether the usage of MEMS in the place of force sensors is feasible. As a matter of fact, detection of static unbalance is usually straightforward for in commerce WBs. Thus, this is the minimum performance requirement, which must be satisfied. On the other hand, detection of pure couple unbalances is usually a hard task. Therefore, it is used to test the capabilities of the newly developed approach.

For each tested unbalance, eight different angular positions are analyzed (Figure 10). The $0\,\mathrm{deg}$ reference point is chosen in order to obtain the initial direction of the rotating sensor reference frame coincident to the fixed one, *i.e.*, as shown by Figure 10, with the z-axis aligned to the WB axis of rotation. For instance, given a zinc tire weight of $10\,\mathrm{g}$ and considering the static unbalance, its effect is analyzed for each angular position of Figure 10. This procedure is followed for both the inner and outer planes of the wheel. Concerning the couple
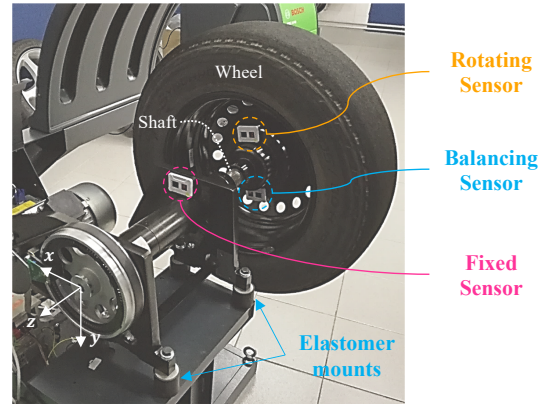

Fig. 9: Detail of the modified WB. The $600\,\mathrm{kN/m}$ (stiffness along y) elastomer mounts are shown together with the XDK sensors locations. A balancing sensor is introduced to counteract the presence of the rotating sensor, which is at a distance of $10\,\mathrm{cm}$ from the axis of rotation.

unbalance, two equivalent tire weights of, *e.g.*, $10\,\mathrm{g}$ are used. The two masses are attached on different wheel planes and in opposite positions, *i.e.*, forming an angle of $180\,\mathrm{deg}$ with each other.

B. Data selection and post-processing

Both accelerations and rotational speeds are characterized by three components measured along $\{x, y, z\}$ directions. First, a post-processing of the acquired data is necessary in order to remove the mean value. Then, the most informative data are selected. As far as the rotating sensor is concerned, the ω_z^R component is neglected because affected by the rotational speed of the WB shaft, which hides the presence of unbalances. As a matter of fact, the z-axis of the rotating sensor is aligned with the WB axis of rotation. As for the fixed sensor, only a_y^F is neglected because characterized by the lower energy content if compared to a_x^F and a_z^F (Figure 11). The same comment applies for a_z^R.
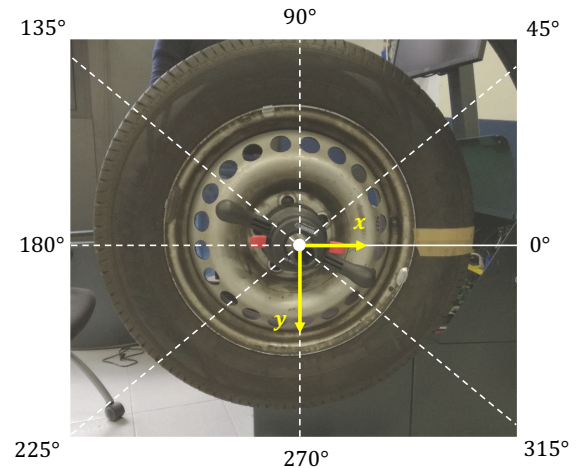

Fig. 10: Minivan test wheel. The considered angular positions are shown. A reference point at $0\,\mathrm{deg}$ is chosen and the initial condition for the rotating XDK sensor reference frame is depicted.
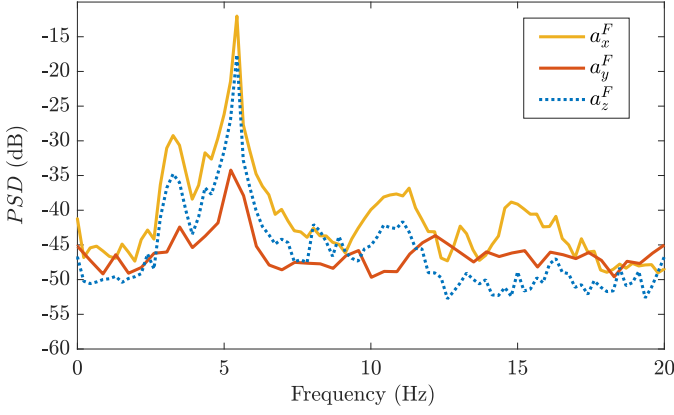
Fig. 11: Spectral analysis of a_x^F, a_y^F, and a_z^F. a_y^F shows the lower energy content. A static unbalance of $60\,\text{g}$ at $0\,\text{deg}$ is considered.
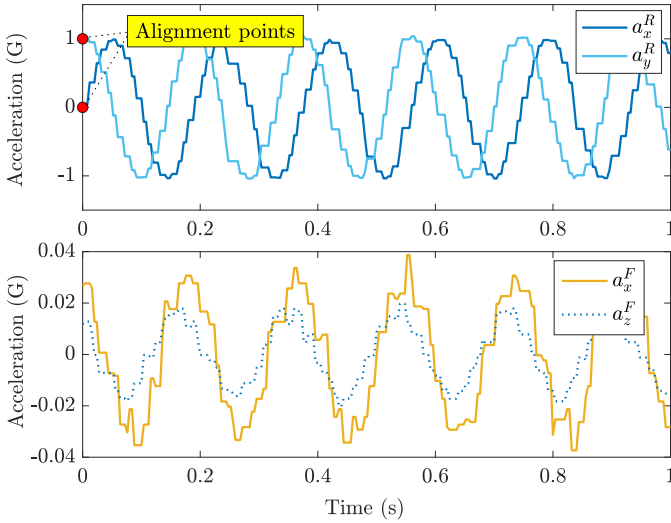

Fig. 12: Data alignment with respect to a_x^R and a_y^R for the fixed sensor acceleration measurements. A static unbalance of $60\,\text{g}$ at $0\,\text{deg}$ is considered.

Accordingly, the following signals are retained for unbalance detection purposes:

- **F**: $a_x^F, a_z^F, \omega_x^F, \omega_y^F, \omega_z^F$;
- **R**: $a_x^R, a_y^R, \omega_x^R, \omega_y^R$.

Before entering the details of the unbalance detection algorithm, data must be aligned with respect to the $0\,\text{deg}$ position of Figure 10. Therefore, a_x^R and a_y^R come to hand. As a matter of fact, x and y components of the rotating sensor acceleration measurements are affected by gravity and, for this reason, they can not be used for unbalance detection. However, they are extremely useful in order to align all the fixed/rotating sensor data with respect to the reference angular position $0\,\text{deg}$. Indeed, when the wheel position is exactly the one of Figure 10, the following condition holds

$$a_x^R(\bar{k}) = 0, \quad a_y^R(\bar{k}) = g_n. \tag{3}$$

with $\bar{k}$ being the alignment time instant and g_n the gravitational acceleration. Therefore, all the data are aligned according to this position. In Figure 12, an illustrative alignment for the fixed sensor acceleration measurements is shown.
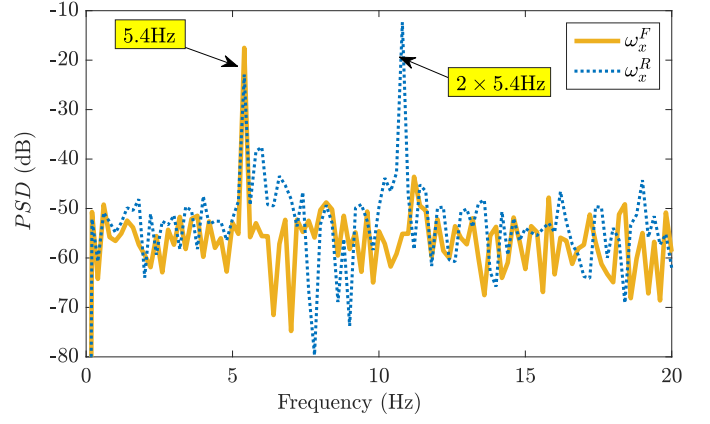

Fig. 13: Spectral analysis of ω_x^F and ω_x^R for a static unbalance of $60\,\text{g}$ positioned at $0\,\text{deg}$. The spectrum of ω_x^R shows two prevalent harmonic components at ω and 2ω.

C. Unbalance detection

To perform an effective balancing, meaningful relationships between acquired data and severity/angular position of unbalances must be retrieved. To this aim, the algorithm is subdivided into two portions. First, the problem of feature extraction is addressed. Then, a regression model is built.

Feature extraction. The goal of the feature extraction step is to condense the information provided by the sensors, *i.e.*, the sequence of N data points, in few variables in order to reduce the computational burden. According to Figure 13, data from gyroscopes and accelerometers show principal harmonic components at the WB rotational speed and at its multiples. Therefore, measured data are fitted by sinusoidal models in order to extract phase and amplitude information. Considering the fixed sensor **F**, the unbalance is seen as an increase in the harmonic component at the frequency of rotation ω [9]. Thus, the following model class is introduced

$$\mathcal{M}_1: \quad \widehat{y}_1(k; [A\ \phi]^T) = A\sin(\omega k T_s + \phi), \tag{4}$$

where A and ϕ are the unknowns, *i.e.*, the amplitude and the phase lag respectively. Looking now at the rotating sensor measurements, the superposition of vibrations at the WB rotational speed and of the rotation of the sensor itself at $325\,\text{rpm}$ leads to an increment of the harmonic component at 2ω. Therefore, the following model is introduced

$$\mathcal{M}_2: \quad \widehat{y}_2(k; [A_1\ A_2\ \phi_1\ \phi_2]^T) = A_1\sin(2\omega k T_s + \phi_1) + \\ A_2\sin(\omega k T_s + \phi_2), \tag{5}$$

where A_1, A_2 and ϕ_1, ϕ_2 are the unknowns, *i.e.*, the amplitudes and the phase lags, respectively. The idea is to fit the data by means of (4) and (5) in order to extract amplitudes and phases of the acquired signals. Models are fit to data relying on nonlinear least squares fitting approaches [16], which minimizes an objective function of the form

$$\min_{\boldsymbol{\beta}} \sum_{k=1}^{N} \left(\widehat{y}_j(k; \boldsymbol{\beta}) - y(k)\right)^2, \tag{6}$$

where $\widehat{y}_j$ ($j = \{1, 2\}$) is the chosen class of models, $\boldsymbol{\beta}$ is a generic column vector containing the unknown parameters, and y is the vector of observations, *i.e.*, $\{a_i^F(k), \omega_i^F(k)\}_{k=1,...,N}$ for (4) and $\{a_i^R(k), \omega_i^R(k)\}_{k=1,...,N}$ for (5), with $i = \{x, y, z\}$. Considering the rotational speed measurements, an illustrative fitting is shown for both the rotating and the fixed sensor in Figure 14. In this scenario, the ω_x component is studied for a static unbalance of $60\,\mathrm{g}$ positioned at $0\,\mathrm{deg}$.

Regression model. Once amplitudes and phases are retrieved from (4) and (5), a regression model linking the extracted features to the actual unbalanced mass is needed. Therefore, two fundamental problems arise:

a) Detection of the unbalance severity;
b) Detection of the unbalance angular position.

The first issue is tackled relying only on amplitudes extracted from the fixed sensor measurements. As a matter of fact, the higher the unbalance severity the higher the magnitude of accelerations and rotational speeds and, consequently, the higher the amplitudes. A preliminary analysis shows that the relationship between amplitudes and unbalance severity can be approximated as linear, no matter which angular position is considered. This fact is shown by Figure 15, considering the ω_x^F measurements. For each tested mass, amplitudes are extracted relying on (4) and (6). Therefore, for each unbalanced mass, different angular positions are tested. Theoretically, for a perfectly balanced wheel, amplitudes should not change in correspondence of variations of the angular position of the unbalance. However, given the fact that the test wheel is a real minivan wheel with asymmetries and imperfections, some dispersion is shown. It is worth to mention that the same linear trend arise for all the acceleration and rotational speed measurements of the fixed sensor. Thus, a linear map $f_m : \mathbb{R}^5 \to \mathbb{R}$ is used to link the amplitudes to the unbalanced mass severity

$$\bar{m} = f_m([A_{a_x^F}\ A_{a_z^F}\ A_{\omega_x^F}\ A_{\omega_y^F}\ A_{\omega_z^F}]) = f_m(\mathbf{A}) =$$

$$= [A_{a_x^F}\ A_{a_z^F}\ A_{\omega_x^F}\ A_{\omega_y^F}\ A_{\omega_z^F}\ 1] \begin{bmatrix} \theta_1 \\ \theta_2 \\ \theta_3 \\ \theta_4 \\ \theta_5 \\ \theta_6 \end{bmatrix} = \mathbf{A}^T \boldsymbol{\theta}, \quad (7)$$

where $A_{a_x^F}, A_{a_z^F}, A_{\omega_x^F}, A_{\omega_y^F}, A_{\omega_z^F}$ are the amplitudes of accelerations and rotational speeds acquired by the fixed sensor. Thus, $\mathbf{A}^T \boldsymbol{\theta}$ forms a hyperplane whose parameters, collected in $\boldsymbol{\theta}$, are unknown and must be identified relying, for instance, on the standard least squares approach (here presented in matrix form) and on $\mathcal{N}$ experiments

$$\boldsymbol{\theta} = (\hat{\mathbf{A}}^T \hat{\mathbf{A}})^{-1} \hat{\mathbf{A}}^T \hat{\mathbf{M}}, \quad (8)$$

where $\hat{\mathbf{A}}$ is a $\mathcal{N} \times 6$ regressor containing the identified amplitudes for each experiment and $\hat{\mathbf{M}}$ is a $\mathcal{N} \times 1$ vector containing the tested unbalanced masses. Thus, $\hat{\mathbf{A}}$ and $\hat{\mathbf{M}}$ are defined as follows

$$\hat{\mathbf{A}} = \begin{bmatrix} A_{a_x^F}^1 & A_{a_z^F}^1 & A_{\omega_x^F}^1 & A_{\omega_y^F}^1 & A_{\omega_z^F}^1 & 1 \\ A_{a_x^F}^2 & A_{a_z^F}^2 & A_{\omega_x^F}^2 & A_{\omega_y^F}^2 & A_{\omega_z^F}^2 & 1 \\ & & \vdots & & \\ A_{a_x^F}^\mathcal{N} & A_{a_z^F}^\mathcal{N} & A_{\omega_x^F}^\mathcal{N} & A_{\omega_y^F}^\mathcal{N} & A_{\omega_z^F}^\mathcal{N} & 1 \end{bmatrix}, \quad \hat{\mathbf{M}} = \begin{bmatrix} m^1 \\ m^2 \\ \vdots \\ m^\mathcal{N} \end{bmatrix} \quad (9)$$

Once the parameters vector $\boldsymbol{\theta}$ is identified, (7) is used to estimate the unbalanced mass $\bar{m}$, given the amplitudes of the measured accelerations and rotational speeds.

Looking now at problem *b)*, the phase lags extracted from the rotating sensor measurements are used. As a matter of fact, given a constant unbalanced mass, variations in its angular position can be detected from the phase lags of the rotational speed measurements. First, the relative quantities, *i.e.*, those computed with respect to the alignment signals a_x^R and a_y^R, are derived as

$$\Delta\phi_{\omega_x^R} = \phi_{a_y^R} - \phi_{\omega_x^R},$$
$$\Delta\phi_{\omega_y^R} = \phi_{a_x^R} - \phi_{\omega_y^R}, \quad (10)$$

where $\phi_{a_x^R}, \phi_{a_y^R}, \phi_{\omega_x^R}$, and $\phi_{\omega_y^R}$ are obtained fitting (5) to the rotating sensor data. As shown in Figure 16, the relationship between $\Delta\phi_{\omega_x^R}$ (or $\Delta\phi_{\omega_y^R}$) and the unbalanced mass angular position is generally nonlinear and it changes depending on the unbalanced mass at hand. For instance, given a static unbalance of $20\,\mathrm{g}$ the relationship becomes linear. Therefore, a
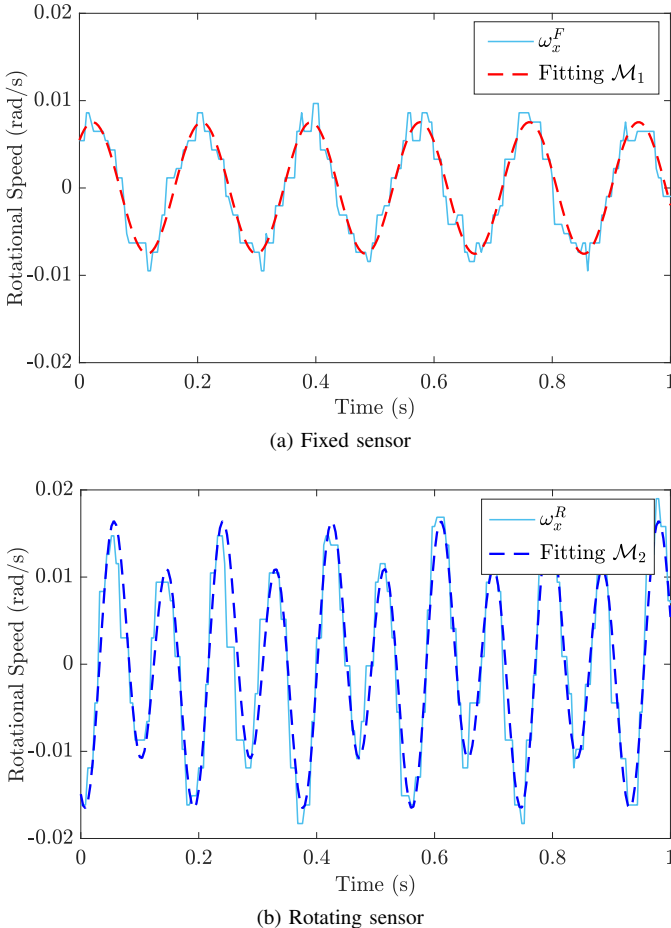

(a) Fixed sensor

(b) Rotating sensor

Fig. 14: Illustrative fitting of ω_x for the fixed (a) and the rotating sensor (b) respectively. A static unbalance of $60\,\mathrm{g}$ at $0\,\mathrm{deg}$ is considered.
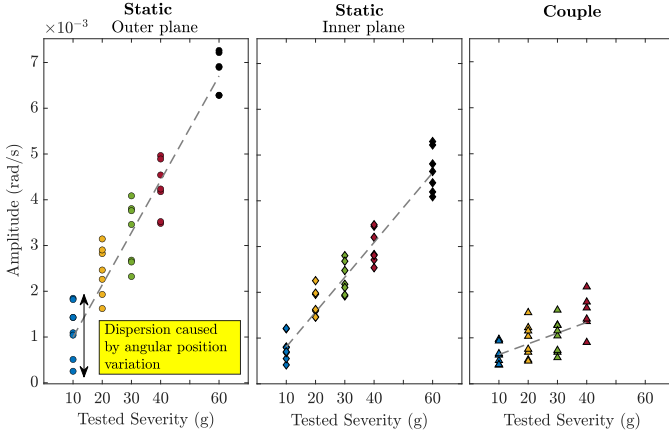
Fig. 15: Amplitude of the rotational speed ω_x^F for the static and the couple unbalance scenarios. The dashed lines highlight the linear trend.
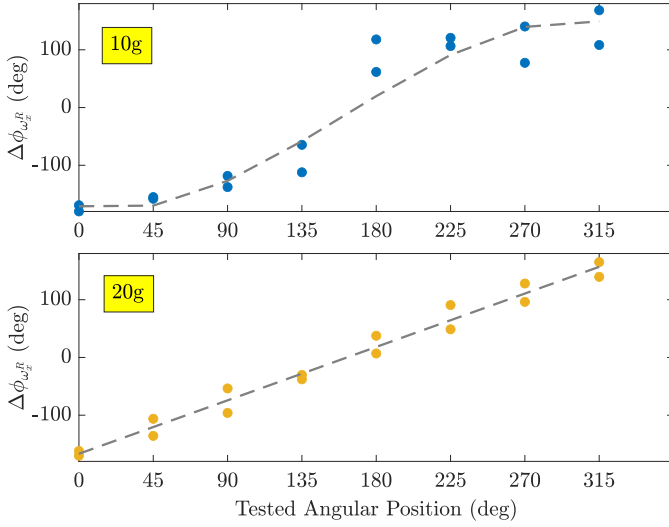

Fig. 16: Phase lags of ω_x^R for static unbalanced masses of 10 and 20 g, respectively. The dashed lines highlight the generally nonlinear trend.

nonlinear map $f_\phi : \mathbb{R}^2 \to \mathbb{R}$ is used to link the relative phase lags to the unbalance angular position (defined with respect to the 0 deg reference point in Figure 10), which can be expressed in the form

$$\bar{\phi} = f_\phi([\Delta\phi_{\omega_x^R} \ \Delta\phi_{\omega_y^R}], \bar{m}) = f_\phi(\boldsymbol{\Delta\phi}, \bar{m}). \qquad (11)$$

As mentioned before, possible changes in (11) depend on the unbalanced mass severity $\bar{m}$, which is retrieved from the linear map (7). Thus, a Neural Network (NN) [17] is trained, for each unbalanced mass $\bar{m}$, in order to model the functional relationship f_ϕ. NN are effective tools for nonlinear regression problems. Therefore, given the time-varying behavior of f_ϕ, which is nonlinear for small unbalanced masses and linear for large ones (see Figure 16), the NN provides the needed flexibility. In Table III, the structure and main parameters of the NN are listed[3]. This configuration leads to good results in terms of prediction error. Given the reduced dataset at hand,

---

[3]The MATLAB *Deep Learning Toolbox™* is used.

Parameters/Hyperparameters	Value/Setting
Activation function	*Sigmoid*
Hidden layers (# neurons)	1 (2)
Learning rate (initial)	0.001
Loss function	*Mean Squared Error (MSE)*
Max. epochs	20 *(static)* − 5 *(couple)*
Optimization algorithm	*Levenberg-Marquardt*
Weights and biases	9

TABLE III: Structure and configuration parameters of the NN.

of 16 samples for the static scenario and of 8 samples for the couple one, the number of epochs (*i.e.*, the maximum number of training iterations) is limited to 20 and to 5, respectively. This allows to train the NN effectively, while avoiding overfitting. Summarizing, the fundamental idea of the algorithm is to first identify the unbalanced mass $\bar{m}$, relying on the linear map (7), and then detect the angular position by means of the NN (11). The overall unbalance detection algorithm is summarized by Figure 17.

VI. EXPERIMENTAL RESULTS

Validation results for the proposed algorithm are shown in Figures 18, 19, and 20. The algorithm is tested for the static and couple unbalance scenarios, considering different severity and angular positions of the unbalanced masses (see Figure 10). It must be noticed that, when the test campaign was performed, only one 60 g zinc tire weight was available. Therefore, this configuration was tested in the static scenario only. Moreover, validation data for some specific angular positions (*e.g.*, 315 deg for the unbalanced mass of 40 g, Figure 18) are not available. For the purpose of this study, the type of unbalance, *i.e.*, static (inner/outer) or couple, is assumed to be known a priori. Since the focus of this work is assessing the effectiveness of MEMS technology for unbalance detection, this is a reasonable assumption. Practically speaking, the distinction between static and couple unbalances can be easily
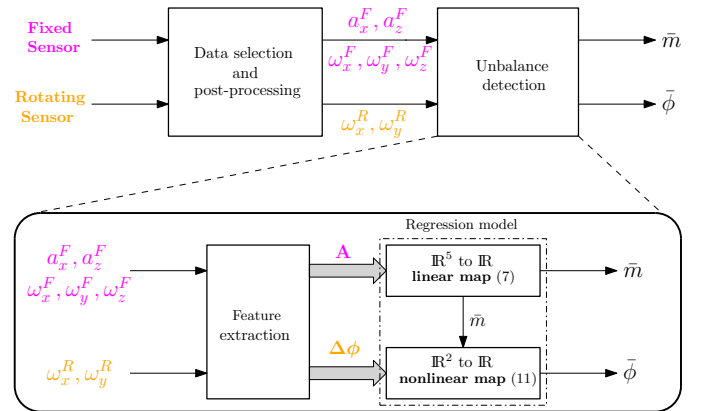

Fig. 17: Unbalance detection algorithm. Given the fixed and the rotating sensor, measured data are depolarized and features, *i.e.*, amplitudes and phases, are extracted. Signals amplitudes are used for unbalance severity detection. Then, given $\bar{m}$, the angular position of the unbalance is obtained relying on a nonlinear map.
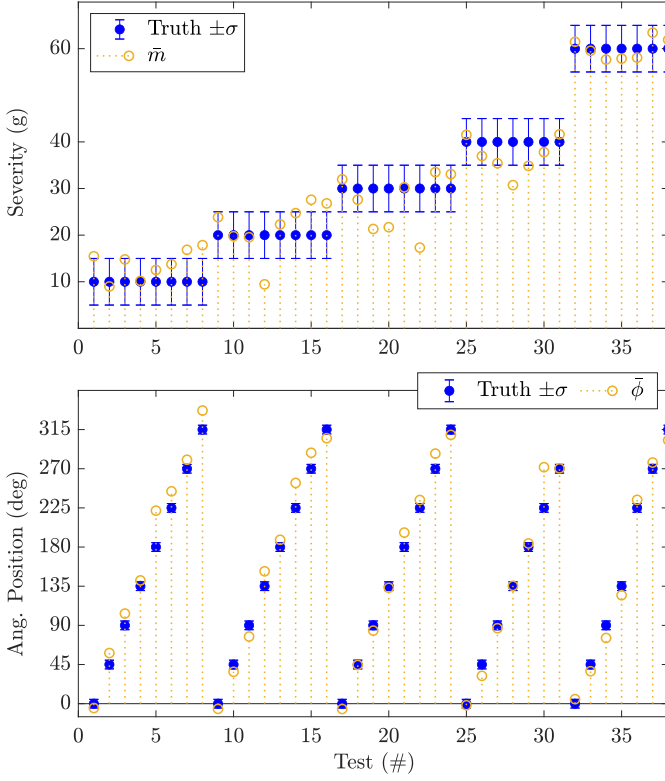
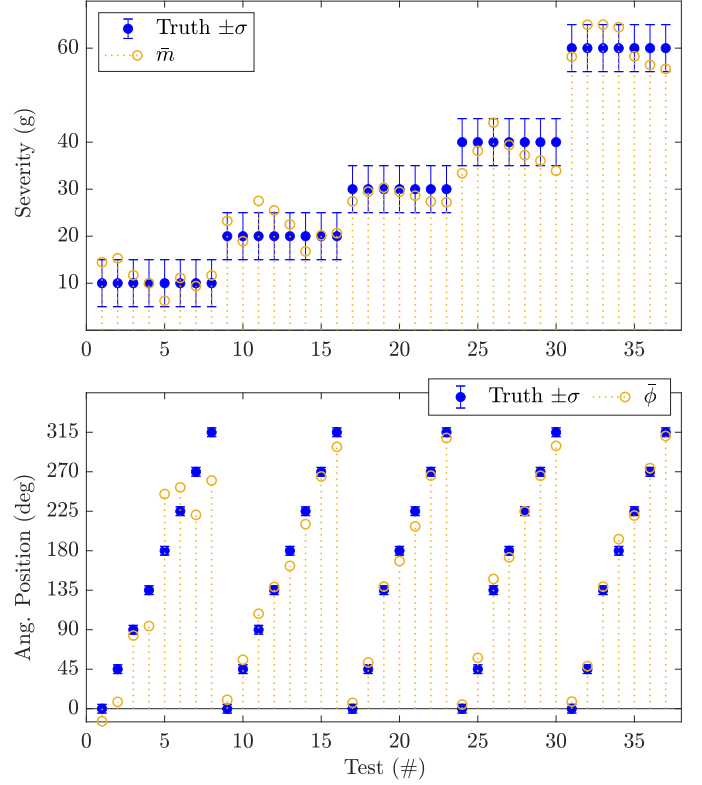Fig. 18: Static unbalance: outer plane validation.

Fig. 19: Static unbalance: inner plane validation.

made in an automatic fashion evaluating the magnitude of the rotational speeds measured by the fixed sensor along the z-axis. As a matter of fact, in case of couple unbalances the ω_z^F magnitude is of order $10^{-4}\,\mathrm{rad/s}$. Conversely, in static unbalance scenarios, values of order $10^{-3}\,\mathrm{rad/s}$ are always measured.

Eventually, in the event of a static unbalance, the algorithm can be used to compute two possible balancing configurations: one for the inner plane and one for the outer plane. Therefore, the user can choose whether to perform the balancing with the inner or the outer plane of the wheel.

In Figures 18, 19, and 20, the *truth*, *i.e.*, the value of the tested unbalanced mass, is represented by the filled dots. To the *truth* is associated a standard deviation σ, which models the precision interval that the WB in commerce possesses in the detection process. In particular, concerning the unbalance severity detection, the standard deviation takes a value of $5\,\mathrm{g}$, *i.e.*, the minimum available balancing weight. Conversely, a value of $5\,\mathrm{deg}$ models the standard deviation for the unbalance angular position detection. This value is consistent with the actually on the market WB level of uncertainty. Thus, we consider that the achieved detection process produces non zero estimation error only if the void circles fall outside the $\pm\sigma$ region. Therefore, from now on detection errors express quantities which are *exceeding* the σ tolerance.

Figures 18 and 19 show the performance for the static unbalance scenario (considering both inner and outer planes of the wheel). As shown in Table IV, the severity detection error, averaged over the different tested angular positions, is at most $1.8\,\mathrm{g}$ for a tested severity of $30\,\mathrm{g}$. Overall, detection
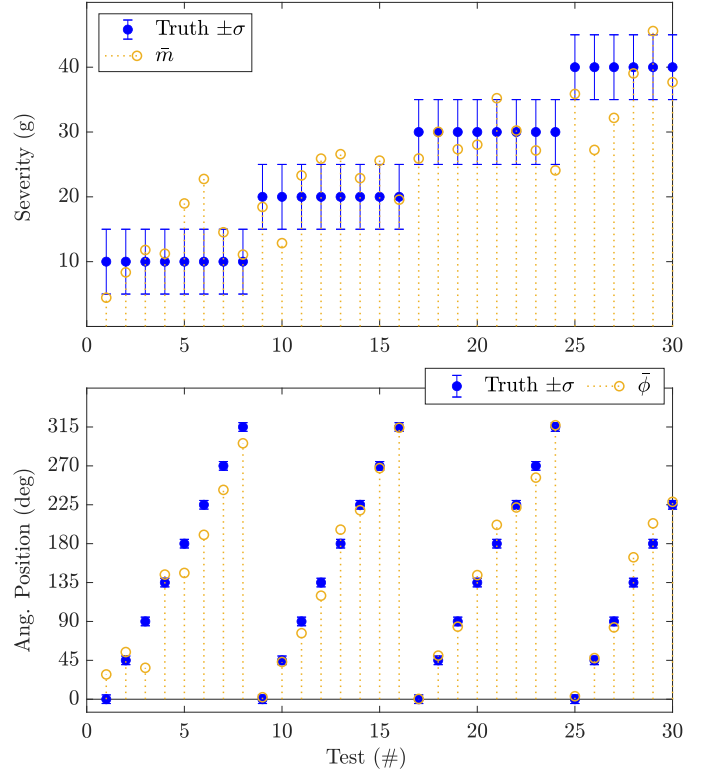

Fig. 20: Couple unbalance validation.

Tested severity (g)	Severity Detection Error (g)		
	Static *Outer plane*	Static *Inner plane*	Couple
10	0.6	0.1	1.5
20	1.2	0.4	0.4
30	1.8	0	0.1
40	0.6	0.4	1.9
60	0	0	NA*
Average	0.8	0.2	1.0

* NA: Not Applicable

TABLE IV: Unbalance severity detection error. The error is averaged over the tested angular positions of Figure 10.

Tested severity (g)	Ang. Position Detection Error (deg)		
	Static *Outer plane*	Static *Inner plane*	Couple
10	11.4	31.9	22.0
20	8.7	7.3	3.9
30	3.9	3.6	3.8
40	7.1	4.1	7.4
60	4.5	1.6	NA*
Average	7.1	9.7	9.3

* NA: Not Applicable

TABLE V: Unbalance angular position detection error. The error is averaged over the tested angular positions of Figure 10.

errors of $0.8\,\mathrm{g}$ and $0.2\,\mathrm{g}$ are guaranteed for the outer and the inner wheel planes, respectively. Therefore, Table V shows the angular position detection error, which is mainly confined to values below $10\,\mathrm{deg}$. Only for a tested severity of $10\,\mathrm{g}$ performance worsen leading to a detection error of $31.9\,\mathrm{deg}$ for the inner wheel plane. As for Figure 20, the performance of the algorithm in the couple scenario is shown (only the pure couple unbalance is considered). In this case, the average severity detection error is still satisfactory, *i.e.*, $1.0\,\mathrm{g}$. While, the average angular position detection error worsen, leading to a value of $9.3\,\mathrm{deg}$. Eventually, the worst performance is still obtained in correspondence of an unbalanced mass of $10\,\mathrm{g}$.

The proposed algorithm guarantees adequate performances in terms of unbalance severity detection. As a matter of fact, the detection error is always confined, on average, below $1.0\,\mathrm{g}$. Therefore, the unbalance is detected correctly for almost all the tested scenarios and the algorithm provides a good indication for the subsequent wheel balancing. As far as the angular position detection is concerned, the performance is highly function of the tested unbalance severity. For both static and couple scenarios, if low unbalances are considered, the angular position detection error rises. Clearly, lowering the unbalanced mass leads to smaller vibrations amplitudes (close to the sensor sensitivity), which brings to a more challenging identification of the signal phases and, consequently, to a worst detection of the angular position. Eventually, to improve the unbalance angular position detection and make the severity detection even more robust, the sensor layout should be modified with more accurate accelerometers and gyroscopes. This would allow for a finer characterization of the vibratory components induced by the unbalances and, consequently, to an improved detection.

In conclusion, starting from the information provided by the proposed algorithm, the wheel balancing is performed according to the steps outlined in Figure 2. Thus, for static unbalances, the balancing weight is attached at $180\,\mathrm{deg}$ with respect to the detected angular position. The same procedure is followed for the couple unbalance, but here two balancing weights are used: one for the inner and one for the outer plane. The exact angular position of the balancing weights may be determined using a protractor, detached from the machine, and measuring angles starting from the $0\,\mathrm{deg}$ reference.

VII. CONCLUSIONS

In this work, the effectiveness of accelerometers and gyroscopes for unbalance detection purposes is proven. By extracting amplitude and phase information from the acquired data, the algorithm is capable of detecting the unbalanced mass with a reasonable accuracy. To do this, an effective mechanical modification of the machine has been proposed, which allows retrofitting existing WBs. As a matter of fact, as shown in Section VI, the approach guarantees an average severity detection error always below $1\,\mathrm{g}$, which is adequate and close to the in commerce WB performance. On the other hand, the average angular position detection error is varying between $7.1\,\mathrm{deg}$ and $14.1\,\mathrm{deg}$, depending whether the static or couple scenario is considered. In particular, low values of unbalanced masses (*i.e.*, $10\,\mathrm{g}$) are generally difficult to detect with a satisfactory accuracy. Eventually, the whole procedure takes less than $5\,\mathrm{s}$, exactly the same time needed for the in commerce WB.

Future works will be focused on improving detection performance especially in the case of low values of unbalanced masses. Moreover, robustness will be increased testing different wheel masses and geometries, in order to provide a general and reliable detection of the unbalance.

APPENDIX A

A brief theoretical insight on the static unbalance is provided to the reader. Consider the mechanical system depicted in Figure 21 and focus on the x-displacement. The motion dynamics is described by the following equation [10]

$$(M + m_r)\ddot{x} + r\dot{x} + kx = m_r\omega^2\varepsilon\sin(\omega t), \qquad (12)$$

where M is the machine mass, m_r the rotor mass, r the damping coefficient, k the spring stiffness, ω the rotational speed, and ε the distance of the rotor center of gravity G from the axis of rotation. The presence of an unbalance in the rotating mass generates a harmonic force at the rotational speed ω.
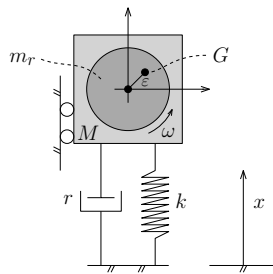
Fig. 21: Unbalanced rotating mass.

REFERENCES

[1] O. F. K. Lund J. W., "Calculations and experiments on the unbalance response of a flexible rotor," *ASME. J. Eng. Ind.*, vol. 89(4), pp. 785–796, 1967.

[2] *Fundamentals of balancing, (3rd ed.)*. Schenck Trebel Corporation, 1990.

[3] H. Schneider, *Auswuchttechnik*, ser. Auswuchttechnik. Springer Berlin Heidelberg, 2007.

[4] D. Norfield, *Practical balancing of rotating machinery*. Elsevier, 2011.

[5] S. Zhou and J. Shi, "Active balancing and vibration control of rotating machinery: a survey," *Shock and Vibration Digest*, vol. 33, no. 5, pp. 361–371, 2001.

[6] N. F. Rieger, "Balancing of rigid and flexible rotors," STRESS TECH-NOLOGY INC ROCHESTER NY, Tech. Rep., 1986.

[7] A. Parkinson, "Balancing of rotating machinery," *Proceedings of the Institution of Mechanical Engineers, Part C: Mechanical Engineering Science*, vol. 205, no. 1, pp. 53–66, 1991.

[8] V. Wowk, *Machinery vibration: balancing*. McGraw-Hill, 1995.

[9] M. MacCamhaoil, "Static and dynamic balancing of rigid rotors," *Bruel & Kjaer application notes, BO*, pp. 0276–12, 2012.

[10] F. Cheli and G. Diana, *Advanced dynamics of mechanical systems*. Springer, 2015.

[11] G. K. Yamamoto, C. da Costa, and J. S. da Silva Sousa, "A smart experimental setup for vibration measurement and imbalance fault detection in rotating machinery," *Case Studies in Mechanical Systems and Signal Processing*, vol. 4, pp. 8–18, 2016.

[12] M. Tarabini and D. Scaccabarozzi, "Uncertainty-based combination of signal processing techniques for the identification of rotor imbalance," *Measurement*, vol. 114, pp. 409 – 416, 2018.

[13] N. Maluf, *An introduction to microelectromechanical systems engineering*. IOP Publishing, 2002.

[14] A. V. Oppenheim, A. S. Willsky, and S. H. Nawab, *Signals and systems 2nd ed*, 1997.

[15] Homberger, "Antivibranti," 2012.

[16] J. E. Dennis Jr and R. B. Schnabel, *Numerical methods for unconstrained optimization and nonlinear equations*. Siam, 1996, vol. 16.

[17] S. Haykin, *Neural networks: a comprehensive foundation*. Prentice Hall PTR, 1994.